ACTA STEREOL 1995; 14/1: 23-28
STERMAT'94
ORIGINAL SCIENTIFIC PAPER

CONDITIONAL WATERSHED SEGMENTATION FOR GRAIN BOUNDARY RECONSTRUCTION

Eric PIRARD, Annick DELANAYE

MICA-Ulg
Université de Liège, Avenue des Tilleuls 45, 4000 Liège, Belgium

ABSTRACT

This paper presents a new approach of watershed extraction in binary images. After a brief reminder about segmentation tools in mathematical morphology, the method, based on the characterisation of contour's points, is detailed. The data used are given by the calypter which is a morphological descriptor incorporating skeleton and contour informations. Then, the advantages of the method are highlighted; in particular, it is shown that the geometrical knowledge, given by the calypter, about the size and configuration of the catchment basins can bring some criteria for the segmentation decision.

Key words: Calypter, image segmentation, mathematical morphology, watershed.

INTRODUCTION

Successful image analysis in materials science relies on efficient image segmentation as much as on unbiased measurements. In recent years, stereology contributed a great deal to the progress in measurement procedures. In order to make such procedures run automatically, it is mandatory to enhance the segmentation process so as to rival with manual segmentation by a human operator.
If we restrain ourselves to the field of geometrical segmentation (as opposed to grey level or colour segmentation), two major problems have to be correctly solved. The first one deals with de-agglomeration of particles in the image of a powder, the second one concerns restoration of grain boundaries in the image of a coherent material. A fundamental difference between these two problems is that particles may overlap while grains always share a common boundary as shown on Fig.1.

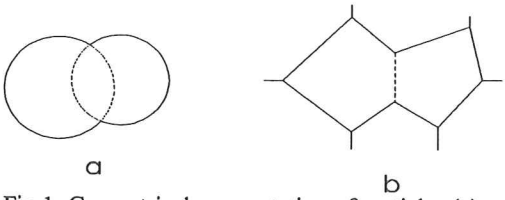

Fig.1. Geometrical segmentation of particles (a) or grains (b).

Among the existing segmentation tools, two distinct approaches can be recognised. The first one identifies remarkable points along a contour and thereafter tries to link these points by considering both the direction and the length of the segmentation lines (Kurdy, 1990). The

second method finds out the ultimate eroded sets and uses them as markers of individual objects. The correct segmentation line is obtained by a geodesic dilatation (Lantuéjoul and Beucher, 1981).This procedure is also called the "watershed segmentation" because the segmentation line is located at the frontier between two catchment basins of a pseudo-relief generated by the distance transform.

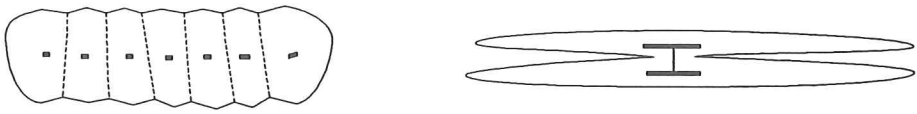

Fig. 2. Over-segmentation due to numerous ultimate eroded components (a) and under-segmentation due to a unique ultimate eroded set (b).

The classical watershed suffers from the lack of stability of the ultimate eroded components. This may lead to over-segmentation as well as to under-segmentation, as shown by Fig. 2.
A gradient operator has been proposed by Vincent and Soille (1991) to merge together neighbouring catchment basins of similar size, while on the other hand the conditional bisector prevents under-segmentation of fibres (Talbot and Vincent,1992). It is the purpose of this paper to show how a combined knowledge of both the contour and the skeleton helps to solve efficiently geometrical segmentation.

METHOD

The Calypter :

The calypter is a morphological descriptor introduced by Pirard (1994) giving for each point of a contour the centre and the radius of its Maximum Inscribed Disc (MID). A calypter is encoded in three steps :

a) Clockwise encoding of the contour points.
b) Holodisc distance transformation.
c) Propagation along the steepest slope from each contour point towards its MID centre.

As opposed to the discrete skeletonization procedures (Meyer, 1989), the calypter strictly encodes those MIDs that are necessary for rebuilding the shape (Fig. 3).
The construction of a watershed dividing line first requires ultimate eroded components to be identified. This would not be a trivial task with the calypter. It appears more efficient to locate landmarks through which the segmentation line is forced to pass. By definition, a watershed dividing line passes through the saddle zone of a relief. Such a zone is identified on a distance function as a region of minimal altitude along the skeleton joining the ultimate eroded sets (cf. minimal skeleton, Meyer, 1989). In accordance with Meyer's terminology, we will call the points belonging to the saddle zone "multiple upstream" points (MU).

Visible MU points :

Clearly, MU points correspond to minima along the radii signal of the calypter. However Fig. 4 indicates that points corresponding to extremities of skeleton branches (X points) share the same property. So, an additional criterion has to be defined to distinguish between concave and convex minima.

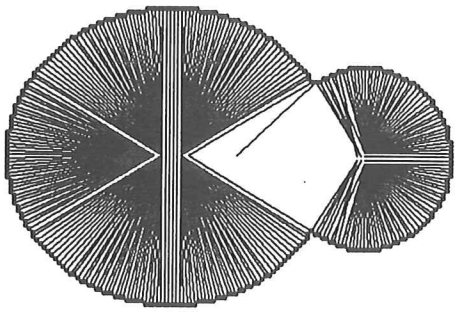

Fig. 3. Visual representation of the calypter of overlapping spheres. Only a small amount of the skeleton points are encoded.

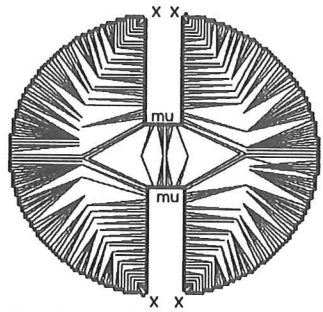

Fig. 4. Local minima of the radii signal correspond either to convexities (X points) or to concavities (MU points).

Let us call A the contour point preceding the sequence of minima along the calypter and P the one immediately following it. If this sequence of minima corresponds to a MU, A and P cannot share a common inscribed tangent disc (Fig. 5a); but if this sequence corresponds to an extremity (X), A and P have to share a common inscribed tangent disc (Fig. 5b). This last property can be proved on the basis of the geometrical information provided by the calypter. Due to digitalisation, MIDs in A and P will be identical only very occasionally. The correct proof is then to search for the smallest of both MIDs and to check whether there exists a disc tangent to the other point whose centre is located less than $\sqrt{2}$ apart. Formally, the proof for a minimum to be a X can be written as follows :

$$\begin{aligned} &\textit{if} \quad \lambda_A \le \lambda_P \qquad \exists\, d^{\lambda}_{P\mathcal{N}_A} \le \lambda_A \\ &\textit{if} \quad \lambda_P < \lambda_A \qquad \exists\, d^{\lambda}_{A\mathcal{N}_P} \le \lambda_P \end{aligned} \qquad \text{(Eq.1)}$$

with λ_A, λ_P : the radius of the MID corresponding to A and P respectively.

$d^{\lambda}_{A\mathcal{N}_P}$: the holodisc distance between A and any point in the 8-connexity neighbourhood of the centre of the MID tangent to the contour in P.

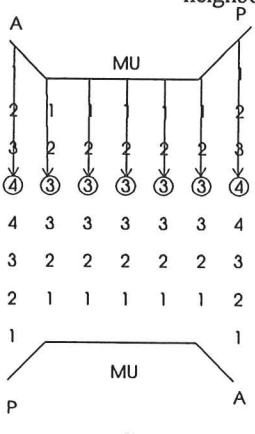

a

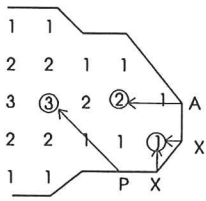

b

Fig. 5. A and P cannot share a common inscribed disc if the minimum is a MU point (a) but if it is a X point, A and P have a common inscribed disc, of radius two on this example (b).

Invisible MU points :

Unfortunately, all the possible MU points of a shape cannot be identified by this simple procedure. In cases where the minimal disc corresponds to a disc unnecessary for the shape reconstruction, the MU is simply invisible from the calypter.
The adequate solution is to take into account what happens during the climbing stage of the calypter encoding. It appears indeed that these MU points give rise to a climbing path that splits and reaches a higher altitude than that of the splitting point on both sides (Fig. 6).

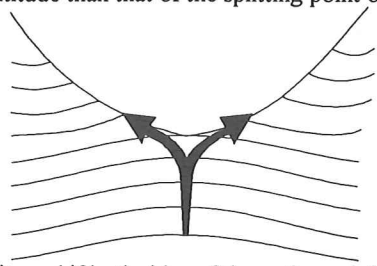

Fig. 6. If a climbing path splits and if both sides of the path reach higher altitudes, the contour point corresponds to a MU.

Doublets of contour points corresponding to pronounced concavities, Fig.7, are also candidates for being MU points. We may consider in such cases that splitting occurs at the contour level so that the only way for locating MU points is to test whether the two points have contiguous MIDs or not (Fig. 8).

Fig. 7. Doublets of concavity points on the chained encoded contour.

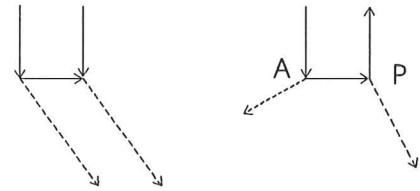

a b

Fig. 8. Doublets of concavity points having contiguous MIDs (a) or separated MIDs (b) corresponding to an invisible MU. The contour is given by a full line; the MIDs are symbolised by their radius in dashed line.

Invisible MU points are easily recorded during the calypter encoding by noting A (P) at the point preceding (following) the invisible MU (Fig.8).

Segmentation line.

Having detected all possible MU points along the contour, the watershed procedure requires to draw a straight line between the MU points that separate the same pair of ultimate eroded sets. In other words, we have to find out two MUs such that their A and P vectors point towards the same pair of catchment basins. Logically, the test to be performed is similar to the identification of a X (Eq.1). Consider Fig. 9; MU_1 is characterised by (A_1,P_1) and MU_2 by (A_2, P_2). Both MU points define a unique watershed dividing line if the pairs A_1, P_2 and A_2, P_1 satisfy relationship (Eq.1).

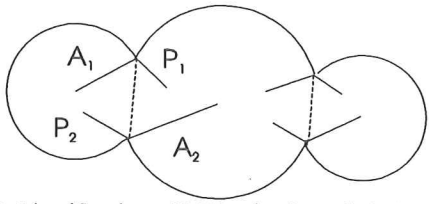

Fig. 9. Identification of MU pairs from their A and P vectors.

DISCUSSION

Up to this point, the classical binary watershed has been exactly automated using the calypter. Notwithstanding a possible gain in processing speed as compared to the usual algorithms, the major interest of segmentation based on the calypter is to gain control over the local geometry of the watershed.

Conditional watershed

Over segmentation due to the existence of numerous disconnections in the ultimate eroded set could be overcome if the width of the neck (length of the dividing line) was compared to the width of the objects. The identification of MU has solved the problem of the computation of ultimate eroded values. These values are given by the maximum radius encountered along the calypter segments belonging to the same catchment basin. To each MU point, we may associate a pair of eroded values : $\left(\lambda_E^A, \lambda_E^P\right)$. Hence, the drawing (or the not drawing) of any segmentation line can be conditioned to a comparison between $\left(\lambda_E^A, \lambda_E^P\right)$ and the neck width ($2\,\lambda_N$), i.e. the distance between the "paired "MU points. A possible condition is:

$$2\lambda_N \leq \gamma \min\left(\lambda_E^A, \lambda_E^P\right) \qquad \text{(Eq.2)}$$

where γ is a user-defined merging intensity (e.g. 80%).

Geometry of the dividing line.

Fig.1 suggests a different approach in segmentation of overlapping objects. This can be achieved by a mitosis splitting the calypter at the paired MU points into two calypters. The geometrical reconstruction of the overlapping regions can be done in several ways by taking into account the geometry of the visible parts. The simplest way is to complete each calypter with the set of points defined by the circular arcs λ_A and λ_P.

Triple points.

In many materials, equilibrium constraints give rise to "triple points" arrangement of grains. The usual watershed segmentation is incorrect because of the existence of four ultimate eroded sets; this method creates an extra triangular particle in the middle (Fig.10).

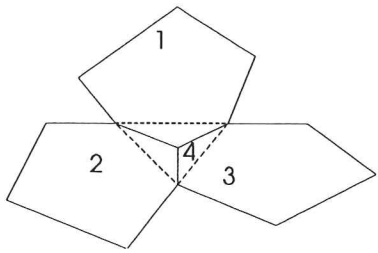

Fig. 10. Representation of three grains (heavy lines) segmented by classical watershed which leads to a triangular configuration of the segmentation. The segmentation based on the calypter can give rise to a more realistic segmentation in star configuration.

With the calypter technique, the false grain generated by three segmentation lines can be located. And thus, the triangle configuration of the segmentation can be transposed into a star one (Fig. 10).

REFERENCES

Kurdy M B. Transformations morphologiques directionnelles et adaptatives. Thèse de doctorat, Ecole des Mines de Paris, 1990.

Lantuéjoul C , Beucher S. On the use of geodesic metric in image analysis. J Microsc 1981; 121: 39-49.

Meyer F. Skeletons and perceptual graphs. Signal Processing, 1989; 16: 335-363.

Pirard E , Nivart J F. New descriptor for skeleton of planar shapes : the Calypter. Non linear image processing V. (SPIE/IST), San Jose, CA, 1994; 2180: 248-259.

Talbot H , Vincent L. Euclidean skeleton and conditional bisectors. Visual Communications and Image Processing' 92 (SPIE), Boston, 1992; 1818: 862-873.

Vincent L , Soille P. Watersheds in digital spaces: an efficient algorithm based on immersion simulations. IEEE Transactions of Pattern Analysis and Machine Intelligence, 1991; 13 (6): 583-598.

ACTA STEREOL 1995; 14/1: 29-34
STERMAT'94
ORIGINAL SCIENTIFIC PAPER

QUANTITATIVE CHARACTERISATION OF WELD SIMULATED STRUCTURES IN DUPLEX STAINLESS STEEL SAF 2205

Jacek Komenda and *Rolf Sandström

Swedish Institute for Metals Research, Drottning Kristinas väg 48,
S-114 28 Stockholm, Sweden
*Professor in Applied Materials Technology, Royal Institute of Technology,
S-100 44 Stockholm, Sweden

ABSTRACT

Microstructures of SAF 2205 type steel after weld simulation were investigated using the automatic image analysis system. Conventional etching produced weak contrast between phases. After modification of the colour etching method, a clear distinction between the austenite and ferrite phases was obtained. Microstructure was quantitatively characterised by the area fraction and the width of austenite at ferrite grain boundaries, also by mean free distance between the austenite islands distributed in the ferrite matrix. The measured structural parameters are related to Charpy-V impact energy data. In particular the width of the austenite islands located at the ferrite grain boundaries had a significant influence on the impact energy.

Keywords: duplex stainless steels, image analysis, impact energy, weld simulation.

INTRODUCTION

Duplex stainless steels possess excellent corrosion resistance, good weldability and good mechanical properties. Modern duplex steels contain approximately the same amounts of ferrite and austenite. This ratio is also maintained in the base metal during welding; however in the heat affected zone (HAZ) the contents of austenite and ferrite depend on the weld thermal cycle. Increasing the austenite content of the weld metal improved tensile ductility and impact toughness (Sridhar et al., 1984). Austenite formation can be suppressed during the welding process resulting in higher ferrite content (Gretoft et al., 1988). Large ferrite grain size and low volume fraction of austenite led to lower impact toughness of the welded material (Enjo et al., 1988). Coarse ferrite grain gave a limited austenite reformation on cooling, with direct consequences for both mechanical properties and corrosion resistance (Ferreira and Hertzman, 1991). Since the relations between ferrite and austenite contents and morphologies are important for the mechanical properties and corrosion resistance of duplex steel weldment, the present paper aims to present a method to determine weld microstructures and to quantitatively characterise them using an automated image processing.

MATERIAL

Weld simulated specimens and impact energy data were used from the earlier work (Cao and Hertzman, 1991). Chemical compositions of steels and Swedish standard specification of SAF 2205 (SS 2377) are given in Table 1. The specimens were the half size Charpy V-notch blanks (5×10×60 mm) machined from the 7 mm plates with the long axes in the rolling direction. Weld simulation was performed on a resistance heated weld simulator with controlled temperature cycles and water cooling. HAZ was located in the centre of the specimen. Table 2 presents the thermal cycles of weld simulation and Charpy-V impact energy data. Specimens were divided into two groups. These with fast cooling rate, (F), were selected into group I. The ones with medium cooling rate, (M), and slow cooling rate, (S), were in group II. Quantitative metallographic examination was performed in HAZ.

Table 1. Chemical composition of steels (charge analysis, wt%) with SAF 2205 specification.

Steel	C	Si	Mn	P	S	Cr	Mo	Ni	N
No. 1	0.024	0.42	1.5	0.024	0.001	22.0	3.0	5.6	0.12
No. 2	0.021	0.40	1.5	0.024	0.001	22.0	3.2	5.7	0.18
No. 3	0.026	0.45	1.9	0.010	0.003	25.1	3.0	5.8	0.17
SS 2377 min.	-	-	-	-	-	21.0	2.5	4.5	0.10
max.	0.050	1.00	2.0	0.030	0.020	23.0	3.5	6.5	0.20

Table 2. Welding simulation thermal cycles and Charpy-V impact energy (tested at room temperature) of investigated specimens, (Cao and Hertzman, 1991).

Group number	Steel	Specimen	Holding time at 1350°C, [s]	Cooling rate, [°C/s]	Impact energy, [J]
I	No. 3	Cr/5/F	5	430	29
	No. 1	N/5/F	5	430	48.5
	No. 2	10/F	10	430	45
	No. 2	5/F	5	430	50
II	No. 2	10/S	10	160	76
	No. 2	10/M	10	300	84
	No. 2	5/S	5	160	89
	No. 2	5/M	5	300	65

ETCHING METHOD

The colour etching method using Beraha II solution (Weck and Leistner, 1983) was modified (Komenda, 1990) to ensure good contrast between ferrite and austenite. A set of three chemicals was prepared in separate vessels: a) 25 ml concentrated hydrochloric acid Hcl; b) 100 ml Beraha etchant that is a mixture of 100 ml Beraha II stock solution (Weck and Leistner, 1983) and 1 g of potassium metabisulphite $K_2S_2O_5$; c) 200 ml of solution: 3 g calcium hydroxide $Ca(OH)_2$ in 200 ml distilled water.

Because of high hydrofluoric acid content, the etchant b) was applied in a plastic vessel and plastic pliers were used to hold the specimen. After grinding, specimens were polished with 3 μm and 1 μm diamond paste and washed in alcohol. Then, without drying, the specimen was immersed in solution a) for 5 seconds, next in b) for 4 seconds and then in c) for 8 seconds. Finally, the specimen was washed in distilled water and then in alcohol. Since the etching was performed at several steps, the method was called stepwise etching.

IMAGE ANALYSIS

Microstructures were investigated using the image analysis system IBAS 2000 (Kontron GmbH/Zeiss, 1986). The area fraction and size of non-metallic inclusions were measured in all specimens. To characterise the content of austenite phase in the specimens of group I, the global area fraction, area fraction at ferrite grain boundaries and area fraction inside the ferrite grains were used. The size of austenite islands inside ferrite grains was measured as circle area equivalent diameter. The mean free distance (MFD) between them was measured according to the formula (Underwood, 1970):

$$MFD = (1-A_\gamma) / N_L \qquad (1)$$

A_γ refers to the global area fraction of austenite and N_L is the number of interceptions of austenite islands per unit length of test lines applied in 0°, 45°, 90° directions to the long axis of the specimen. The width of elongated austenite islands at ferrite grain boundaries was measured using two parameters. The average value of intercept length from the horizontal test lines represented random width of the austenite island, W_h. The second parameter, W_b , was obtained from the measurement of two distances perpendicular to each other, based on the areal moments of inertia (Kontron GmbH/Zeiss, 1986). For the ellipsoidal austenite island the size of major and minor axes were obtained. The minor axis size

was the width of an austenite island, W_b. Fig. 1 illustrates the measurement principles for W_h and W_b .

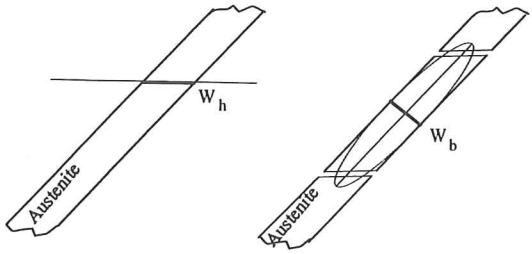

Fig. 1. The principles of the width measurement methods (W_h and W_b respectively) applied to the austenite phase located along the ferrite grain boundaries.

To measure W_b long austenite islands were cut into sections. It was achieved by subtraction of an image with horizontal lines from a binary image of the structure. The principles of image processing are shown in Fig. 2. The austenite in specimens of group II was characterised by the global area fraction, mean free distance (MFD) and circle area equivalent diameter. The last parameter was applied to the austenite agglomerates (here called packages), showing a Widmannstätten type structure.

RESULTS

No post-welding inclusions were present in the structure. Some amount of silicates and sulphides was measured: 0.13 vol% in Cr/5/F and N/5/F and from 0.05 to 0.07 vol% in the remaining specimens. The average size of inclusions was from 2.2 to 2.8 μm. Figs. 3a to 3h present examples of investigated microstructures. With decreasing cooling rates the austenite phase first nucleated at ferrite grain boundaries, next grew inside grains as needles and then austenite particles appeared inside ferrite grains. Widmannstätten type structures are shown in Figs. 3f and 3h. The largest ferrite grains (234 μm) were in 10/F specimen. Cr/5/F, N/5/F and 5/F had grains with a mean size of 153 μm, 203 μm and 159 μm respectively. Grains were equiaxed. Austenite area fraction, mean free distance, width of islands located at ferrite grain boundaries (W_h and W_b) and the size of austenite islands inside ferrite grains are given in Table 3. Table 4 presents austenite characteristics measured in specimens of group II. Under similar thermal cycles the lowest austenite content was measured in steels that contained more Cr and less N in comparison to the SAF 2205 specification. Slow cooling produced more austenite and the width of austenite at ferrite grain boundaries was larger. W_h and W_b parameters showed strong relation to each other with a regression coefficient 0.97 . Since the measurement of W_b is more time consuming, the W_h parameter was applied in further analysis. No effect of the ferrite grain size on Charpy-V impact energy tested at room temperature was found, although this was anticipated from the literature information (Enjo et al., 1988). The larger the ferrite grain size, the lower should the impact energy be but in the present work this effect was not observed. However, a clear relation with a correlation coefficient of 0.90 was noted between the austenite area fraction A_γ and impact energy C_V :

$$C_V = a + b \times A_\gamma \quad (2)$$

where a = 31 [J] and b = 1.9 [J/% austenite].

Even stronger correlation was found between the width of the austenite phase located at the ferrite grain boundaries and the impact energy. Fig. 4 presents this relation for the specimens of group I. The correlation coefficient was 0.97 and the following equation was obtained from the regression analysis:

$$C_V = a + b \times W_h \quad (3)$$

where a = 17.6 [J] and b = 7.8 [J/μm].

The relation between impact energy and the size of austenite particles inside ferrite grains showed a correlation coefficient value of 0.68 .

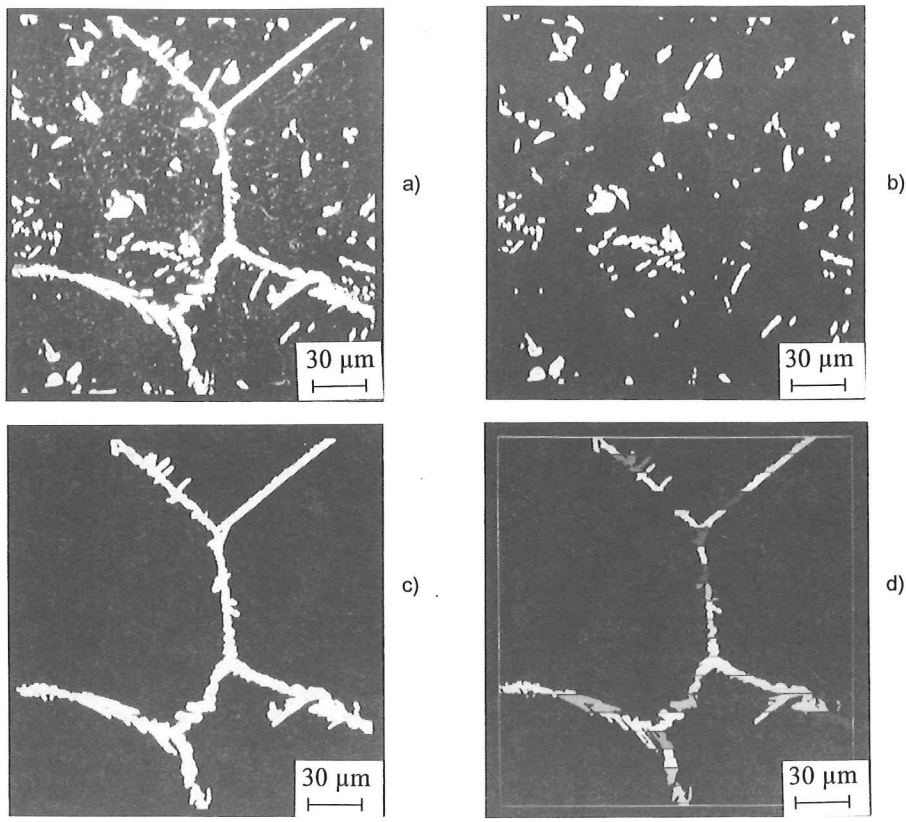

Fig. 2. Image processing steps for ferrite - austenite structure: a) original image, (etched structure), b) binary image of austenite inside ferrite grains, c) austenite at ferrite grain boundary, d) austenite at ferrite grain boundary cut by subtracted line pattern.

Table 3. Mean values of parameters measured on austenite phase in specimens of group I.

Specimen	Area fraction, %			Mean free distance µm	Width, W_h µm	Width, W_b µm	Island size inside grains µm
	global	at ferrite grain boundaries	inside grains				
Cr/5/F	1.0	0.8	0.2	152	1.5	1.6	2.5
N/5/F	3.7	2.1	1.6	67	3.6	3.2	3.3
10/F	10.9	3.5	7.4	24	3.9	4.2	4.2
5/F	12.5	5.9	6.6	21	4.1	4.0	3.4

DISCUSSION

The amount and distribution of the austenite phase was found to be the main factor controlling the impact energy of weld simulated specimens. A lower austenite content has been measured in specimens that contained less nitrogen and more chromium, respectively. The holding time at peak temperature during weld simulation did not affect the amount of austenite but the cooling rate did. With the lower cooling rate the specimens contained more austenite. The area fraction and size of inclusions varied in a too narrow range to show the effect on impact energy. Nor the results did not show any relation between ferrite grain size and impact energy. It was assumed due to a stronger influence of the auste-

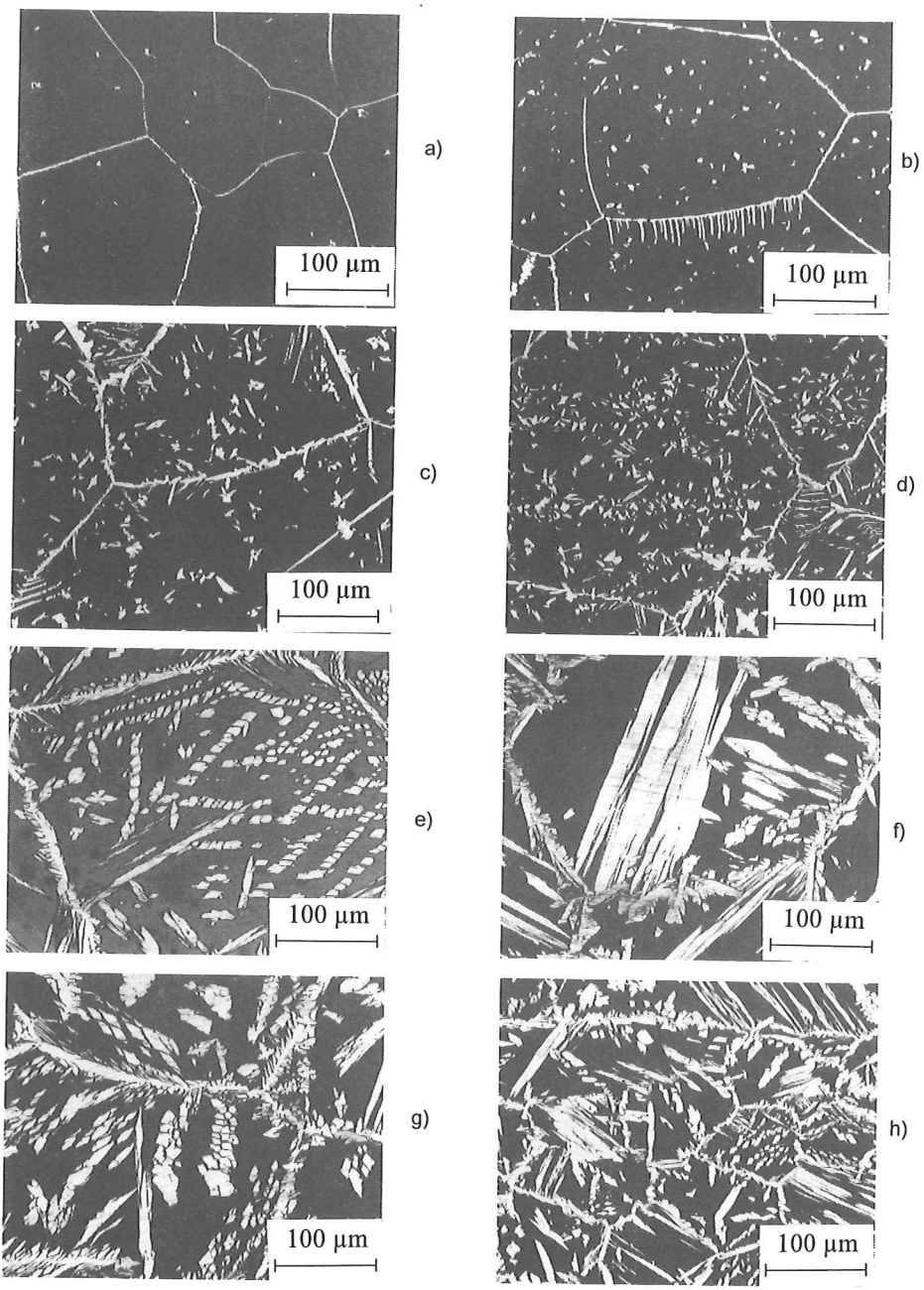

Fig. 3. Investigated microstructures of duplex stainless steel weldment (HAZ).
a) Cr/5/F, b) N/5/F, c) 10/F, d) 5/F, e) 10/S, f) 10/M, g) 5/S, h) 5/M.

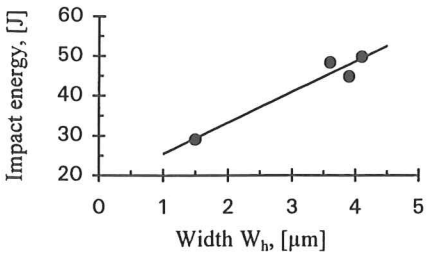

Fig. 4. Charpy-V impact energy versus width of austenite at ferrite grain boundaries.

Table 4. Mean values of parameters measured on austenite phase in specimens of group II.

Specimen	Area fraction %	Mean free distance μm	Package size μm
10/S	21.0	20	54
10/M	24.9	19	59
5/S	25.6	18	94
5/M	26.5	15	71

nite content and distribution on the impact properties. A very strong relation was found between the width of austenite located at ferrite grain boundaries and impact energy. The relation between the mean free distance of austenite islands and impact energy was not very much pronounced. An attempt to describe the austenite packages quantitatively in specimens of group II was made, where the IBAS system was applied in a semi-automatic way. However, the general measurements were performed in automatic way and the time of work was relatively short concerning the amount of information.

CONCLUSIONS

The etching method presented in the paper provides a clear distinction between austenite phase and ferrite matrix. In agreement to the literature information a pronounced correlation was observed between the austenite content and impact energy. The width of the austenite located at ferrite grain boundaries showed a relation to the Charpy-V impact energy of the weld simulated specimens. As the width of austenite increased, so did the impact energy. This relation was found to be stronger than the one between austenite content and impact energy, indicating that the austenite in ferrite grain boundaries plays a special role.

ACKNOWLEDGEMENTS

The project was performed within the General Research Programme at the Swedish Institute for Metals Research and the financial support is gratefully acknowledged. The authors thank Dr Staffan Hertzman, Swedish Institute for Metals Research, for supplying the specimens and impact test data.

REFERENCES

Cao HL, Hertzman S. The relationship between impact properties and welding simulated microstructures in three duplex stainless steels. In: Proc Int Conf Duplex Stainless Steels, Beaune France, 1991.

Enjo T, Kuroda T, Imanishi R. Microstructure and toughness in weld heat affected zone of duplex stainless steel. Transactions of JWRI 1988; 17/2: 105-111.

Fereira PJ, Hertzman S. δ-ferrite grain growth in simulated high temperature HAZ of three duplex stainless steels. In: Proc Int Conf Duplex Stainless Steels, Beaune France, 1991.

Gretoft B, Rigdal SL, Karlsson L, Svensson LE. Influence of welding process on mechanical properties of duplex stainless steel weld metals. In: Proc Conf Stainless Steels '87, Stockholm Sweden, 1988.

Komenda J. Quantitative characterization of weld simulated microstructures in the duplex stainless steel SAF 2205. Swedish Institute for Metals Research report IM-2581, 1990.

Kontron GmbH/Zeiss, IBAS - The Interactive Image Analysis System, Eching, Germany, 1986.

Sridhar N, Flasche LH, Kolts J. Corrosion and mechanical properties of duplex stainless steel weldments. In: Developments in stainless steel technology, Detroit, Metals Park, ASM, 1985: 341.

Underwood E. Quantitative Stereology. Addison-Wesley Publ Co , 1970: 82-83.

Weck E, Leistner E. Metallographic instruction for colour etching by immersion, Part II: Beraha colour etchants and their different variants. DVS, 1983.